ARTICLE IN PRESS

Materials Science & Engineering A ▮ (▮▮▮▮) ▮▮▮–▮▮▮

Contents lists available at SciVerse ScienceDirect

Materials Science & Engineering A

journal homepage: www.elsevier.com/locate/msea

Magnetic freeze casting inspired by nature

Michael M. Porter [a,*], Michael Yeh [b], James Strawson [b], Thomas Goehring [b], Samuel Lujan [b], Philip Siripasopsotorn [b], Marc A. Meyers [a,b], Joanna McKittrick [a,b]

[a] Materials Science and Engineering Program, University of California, San Diego, 9500 Gilman Dr., La Jolla, CA 92093, USA
[b] Department of Mechanical and Aerospace Engineering, University of California, San Diego, 9500 Gilman Dr., La Jolla, CA 92093, USA

ARTICLE INFO

Article history:
Received 11 July 2012
Accepted 13 July 2012

Keywords:
Bio-inspired
Freeze casting
Magnetic alignment
Ceramic scaffold

ABSTRACT

Magnetic field aligned freeze casting is a novel method to fabricate porous, anisotropic ceramic scaffolds with a hierarchy of architectural alignment in multiple directions. A weak rotating magnetic field applied normal to the ice growth direction in a uniaxial freezing apparatus allowed the manipulation of magnetic nanoparticles to create different pore structures and channels with long-range order in directions parallel and perpendicular to the freezing direction. Porous scaffolds consisting of different host ceramics (hydroxyapatite (HA), ZrO_2, Al_2O_3, or TiO_2) mixed with varying concentrations (0–9 wt%) of Fe_3O_4 nanoparticles were fabricated by freeze casting under three different conditions: (1) no magnetic field, (2) a static magnetic field of 0.12 T, or (3) a rotating magnetic field of 0.12 T at 0.05 rpm. The HA, ZrO_2, and Al_2O_3 scaffolds showed biphasic material properties with separate Fe_3O_4-rich and Fe_3O_4-poor regions. The TiO_2 scaffolds showed homogeneous distributions of Fe_3O_4 throughout the macrostructures, which resulted in aligned pore channels parallel to the magnetic field, normal to the ice growth direction. In the magnetic field direction, the compressive strength and stiffness of the TiO_2 scaffolds containing Fe_3O_4 was doubled. The enhanced mechanical performance of the field aligned TiO_2 scaffolds are the result of the long-range microstructural order in multiple directions—(1) the magnetic field direction and (2) the ice growth direction.

1. Introduction

A common unifying theme in the study of natural materials is the presence of anisotropy and architectural hierarchy over multiple length scales [1,2]. This type of directional order allows biomaterials to be lightweight, high strength, and multifunctional [3]. Abalone nacre and bone, for instance, are structural materials with exceptional mechanical properties designed for body support; and, impact resistance in the case of nacre, or blood flow and joint movement in the case of bone [4,5]. These properties result from highly ordered, structural alignment in multiple directions across several length scales. In the field of bio-inspired design, many new technologies to fabricate high-performance, multifunctional materials that mimic the nano-/micro-structural features of natural materials are being explored with varying success.

Of these, freeze casting has become a most promising new technique to fabricate porous ceramic scaffolds [6,7]. Potential applications range from bone replacements [8–10] and tough hybrid composites (upon infiltration of a second phase) [10–13], to separation filters, insulators, catalyst supports, or piezoelectric devices [7,14–17]. Freeze casting of ceramics is a physical process in which an aqueous slurry composed of a solid phase (e.g., ceramic powder) and a fugitive liquid carrier (e.g., water) is directionally frozen in a mold, then sublimated to remove the frozen liquid phase, and finally sintered to partially densify and strengthen the green constructs [6,7,18]. During the freezing process, ceramic particles are pushed between and trapped within growing lamellar ice crystals [6,7,18]. The thermodynamics that govern the phenomena of particle rejection and entrapment are explicated by Wegst et al. [18] and Deville et al. [19], where constitutional supercooling drives instabilities (or undulations) in the freezing front that lead to the nucleation and growth of well-ordered, interconnected ice channels. Intricate microstructural features, such as surface roughness, wall thickness, pore geometry and inter-lamellar bridging, may be controlled by altering the slurry properties or changing the freezing direction and solidification kinetics [8–10, 20–30]. An inherent drawback of these scaffolds is their lack of strength and stiffness transverse to the direction of ice growth. That is, the outstanding mechanical properties usually celebrated in these materials only exist in a single uniaxial direction, parallel to the freezing direction [27]. For many applications, this may not be problematic. However, applications such as bone replacements or tough

---

[*] Corresponding author. Tel.: +1 757 615 3929; fax: +1 858 534 5698.
E-mail address: m1porter@ucsd.edu (M.M. Porter).

0921-5093/$ - see front matter © 2012 Elsevier B.V. All rights reserved.
http://dx.doi.org/10.1016/j.msea.2012.07.058

hybrid composites that require substantial mechanical performance in multiple directions may not be well-suited by conventional freeze casting.

Some attempts to introduce greater microstructural control have been previously reported. Fu et al. [9] and Munch et al. [27] used additives, such as glycerol, dioxane, ethanol or sucrose, to modify the microstructure (e.g., lamellar or cellular) and surface roughness (e.g., smooth or dendritic) of freeze-cast scaffolds by changing the eutectic phase diagram of the colloidal suspensions. Munch et al. [27] showed that patterning the freezing surface can manipulate the long-range ordering of ice lamellae by controlling the initial direction of nucleation. Zhang et al. [31] fabricated dense/porous bilayered ceramics by applying an electric field during freezing. Moon et al. [22], Macchetta et al. [24], and Koh et al. [25,30] demonstrated the concept of radial cooling to construct porous ceramics with radial channel alignment. Regardless, none of these modifications have been shown to significantly enhance the mechanical properties in planes normal the ice growth direction. New additions to conventional freeze casting techniques that may align microstructural features and increase the strength and stiffness in multiple directions are still of great interest.

One mechanism commonly used to align small-scale materials, such as carbon nanotubes or ferrous nanoparticles, is an external magnetic field [32–38]. Magnetic fields are particularly useful in materials fabrication when physical barriers, such as the walls of a mold, restrict the manipulation of materials through direct contact. In ceramics processing, high magnetic fields (>10 T) have been shown to control the texture of feeble magnetic ceramics, such as HA, Al_2O_3, or TiO_2 [39–45]. Unfortunately, high magnetic fields are produced by special superconducting magnets that are infeasible in most laboratories due to their high cost, high energy consumption, and safety concerns [34]. In contrast, small magnetic particles such as magnetite (Fe_3O_4) are known to aggregate into linear-chain clusters in the direction of relatively weak magnetic fields (<1 T) [36,38,46]. Mashkour et al. [34] showed that it is possible to align cellulose fibers doped with Fe_3O_4 using a permanent magnet with a field strength <0.18 T. Using this concept, low magnetic fields may align the complex microstructures in freeze-cast ceramics containing small amounts of Fe_3O_4.

Inspired by the helicoidal structure of the narwhal tusk, an external rotating magnetic field was applied to a conventional freeze casting system for the first time. A permanent neodymium magnet and cast iron flux path distributors were used to direct a magnetic field perpendicular to the ice growth direction. Porous scaffolds with structural alignment in both the longitudinal (i.e., ice growth direction) and transverse (i.e., magnetic flux direction) planes were fabricated from nonmagnetic ceramic powders mixed with small amounts of Fe_3O_4 nanoparticles. The compressive mechanical properties of the scaffolds were measured in directions perpendicular and parallel to the magnetic flux path and freezing directions. This work introduces the novel concept of magnetic freeze casting and explains its potential as a simple, low cost processing method to fabricate porous, anisotropic ceramic scaffolds with a hierarchy of architectural alignment in multiple directions.

2. Materials and methods

2.1. Magnetic freeze casting setup

Samples were prepared using a custom built freeze casting unit and rotating permanent magnet. Fig. 1 shows a picture of the magnetic freeze casting setup. The freeze casting unit consists of a copper cold finger immersed in a liquid nitrogen bath. A band heater and thermocouple linked to a PID controller are attached to the copper cold finger in order to control the cooling rate of the copper surface at the bottom of a polyvinyl chloride (PVC) mold with a 20 mm inner diameter. The rotating permanent magnet is constructed from a 1.32 T neodymium rare earth magnet, grade N42 ($2.5\times10\times10$ cm^3) (Applied Magnets, Plano, TX). Two cast iron channel arms, threaded stainless steel rods, and cast iron flux path distributors are attached to the neodymium magnet to direct and concentrate the magnetic flux path through the PVC mold perpendicular to the ice growth direction (*Z*-axis). The magnetic field strength can be varied from 0 to 0.15 T by adjusting the distance of the flux path distributors with the threaded rods. The permanent magnet device was hung by a vertical aluminum shaft connected to a 3 V, 1.6 A, 233 oz-in geared bipolar stepper motor (RobotShop Inc., Swanton, VT), controlled by an electronic user

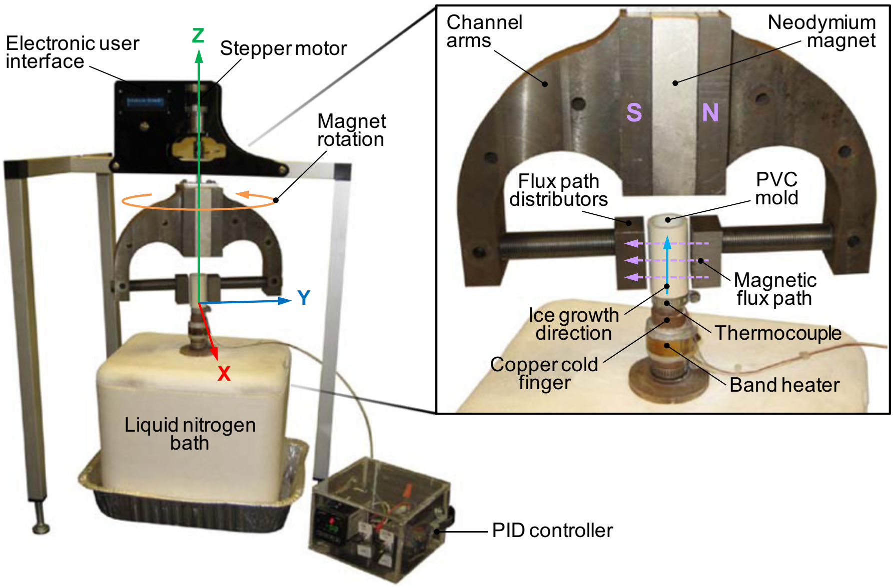

Fig. 1. Magnetic freeze casting setup, illustrating the magnet rotation, ice growth, and magnetic flux path directions. The direction normal to the ice growth (*Z*-axis) and magnetic flux path (*Y*-axis) directions is represented by the *X*-axis.

Please cite this article as: M.M. Porter, et al., Magnetic freeze casting inspired by nature, Materials Science & Engineering A (2012), http://dx.doi.org/10.1016/j.msea.2012.07.058

interface, Arduino Uno-R3 (SparkFun Electronics, Boulder, CO), capable of rotating the magnet 0.05–0.50 rpm about the *Z*-axis. Finite element models (FEM) of the magnetic flux path distributions were developed using the software, FEMM 4.2 (David Meeker, Waltham, MA).

2.2. Sample preparation

Aqueous slurries of 10 vol% HA (Trans Tech, Adamstown, MD), ZrO_2 (Sigma Aldrich, St. Louis, MO), Al_2O_3 (Sigma Aldrich, St. Louis, MO), or TiO_2 (Sigma Aldrich, St. Louis, MO) powders were mixed with varying concentrations of 0–9 wt% (0–8 vol% of the total solids) Fe_3O_4 nanoparticles (Sigma Aldrich, St. Louis, MO). Table 1 shows the physical properties of the ceramic powders, as received. All slurries contained 1 wt% of each: organic binders, polyethylene glycol (PEG) (Alfa Aesar, Ward Hill, MA) and polyvinyl alcohol (PVA) (Alfa Aesar, Ward Hill, MA), and an ammonium polymethacrylate anionic dispersant, Darvan® 811 (R. T. Vanderbilt Company, Inc., Norwalk, CT). The slurries were ball milled in an alumina grinding medium for 24 h, followed by degassing under low vacuum for 10–20 min. Approximately 10 mL of the degassed slurries were poured into the PVC mold and frozen at a constant rate of 10 °C/min. Samples were frozen under three different magnetic field conditions: (1) no magnetic field; (2) a static magnetic field of 0.12 T; and (3) a rotating magnetic field of 0.12 T at 0.05 rpm. After freezing, the samples were removed from the mold with a hydraulic press and lyophilized in a bench-top freeze dryer (Labconco, Kansas City, MO) at −50 °C and 350 Pa for 72 h. The porous green constructs were then sintered in an open air furnace for 3 h at predetermined temperatures of 1300 °C for HA and ZrO_2, 1500 °C for Al_2O_3, and 900 °C for TiO_2 with heating and cooling rates of 2 °C/min.

2.3. Material characterization

The relative density (ρ_{rel}) and porosity (ϕ) of the scaffolds were measured by mass (m) and volume (V) with respect to that of a fully dense material of equal composition (ρ'), as shown in Eqs. (1) and (2):

$$\rho_{rel}=\frac{\rho}{\rho'}=\frac{m/V}{\gamma\rho'_{Fe_3O_4}+(1-\gamma)\rho'_{host}} \tag{1}$$

$$\phi=(1-\rho_{rel})\times 100\% \tag{2}$$

where $\rho=m/V$ is the measured sample density, $\rho'_{Fe_3O_4}$ and ρ'_{host} are the densities of fully dense Fe_3O_4 and host ceramic (HA, ZrO_2, Al_2O_3, or TiO_2), respectively, and γ is the weight fraction of Fe_3O_4. The average pore sizes and channel widths of the scaffolds were measured using ImageJ software. Table 3 lists the average densities and porosities of the TiO_2 scaffolds.

Energy-dispersive X-ray spectroscopy (EDX) was performed with a Philips XL30 field emission environmental scanning electron microscope (FEI-XL30, FEI Company, Hillsboro, OR). The samples were coated with iridium using an Emitech K575X sputter coater (Quorum Technologies Ltd., West Sussex, UK). Elemental mapping and analyses were performed at 20 kV using an Oxford EDX attachment and Inca software.

X-ray diffraction (XRD) was performed with a Miniflex II XRD machine (Rigaku, The Woodlands, TX) to confirm the crystal systems of the as-received ceramic powders (Table 1) and characterize the crystal structures of the TiO_2 scaffolds before and after sintering.

2.4. Micro-computed tomography (μCT)

Two TiO_2 scaffolds containing 3 wt% Fe_3O_4, made with (1) no magnetic field and (2) a rotating magnetic field of 0.12 T at 0.05 rpm, were scanned on a micro-computed tomography (μCT) unit, Skyscan 1076 (Skyscan, Kontich, Belgium). The scaffolds were positioned inside a Styrofoam tube and imaged at 9 μm isotropic voxel size, applying an electric potential of 70 kVp and a current of 200 μA, using a 1 mm aluminum filter. A beam hardening correction algorithm was applied during image reconstruction. Images and 3D rendered models were developed using Skyscan's Dataviewer and CTVox software.

Table 1
Properties of ceramic powders, as received. Information reported by manufacturers unless otherwise noted.

	Magnetite (Fe_3O_4)	Hydroxyapatite (HA)	Zirconia (ZrO_2)	Alumina (Al_2O_3)	Titania (TiO_2)
Crystal system[a]	Cubic	Hexagonal	Monoclinic	Hexagonal	Tetragonal
Density (g/cm^3)	4.95	3.15	5.89	4.00	4.26
Molar mass (g/mol)	231.53	502.31	123.22	101.96	79.87
Particle size (μm)[b]	< 0.05	1–3	0.2–0.5	2–5	0.2–0.5

[a] Crystal systems confirmed by XRD measurements.
[b] Particle sizes measured from SEM micrographs.

Table 2
Elemental analysis of sintered HA, ZrO_2, Al_2O_3, and TiO_2 scaffolds containing 3 wt% (~3 vol%) Fe_3O_4 made with a static magnetic field of 0.12 T, showing the concentration (wt%) of iron (Fe) and host elements (Ca, P, Zr, Al, Ti, O) in the Fe_3O_4-rich (edge) and Fe_3O_4-poor (center) regions of the scaffolds.

	Hydoxyapatite (HA)		Zirconia (ZrO_2)		Alumina (Al_2O_3)		Titania (TiO_2)	
	Element	(wt%)	Element	(wt%)	Element	(wt%)	Element	(wt%)
Fe_3O_4-rich Region	Fe	5.78	Fe	8.27	Fe	7.83	Fe	1.64
	Ca	36.56	Zr	61.29	Al	47.40	Ti	61.07
	P	15.83	O	30.44	O	44.77	O	37.29
	O	41.82	–	–	–	–	–	–
Fe_3O_4-poor Region	Fe	0.08	Fe	0.20	Fe	0.33	Fe	1.61
	Ca	45.89	Zr	71.17	Al	51.69	Ti	61.65
	P	15.29	O	28.62	O	47.98	O	36.74
	O	38.73	–	–	–	–	–	–

Please cite this article as: M.M. Porter, et al., Magnetic freeze casting inspired by nature, Materials Science & Engineering A (2012), http://dx.doi.org/10.1016/j.msea.2012.07.058

Table 3
Density, porosity, and compressive mechanical properties of TiO_2 scaffolds containing 1–9 wt% (0–8 vol%) Fe_3O_4 made with no magnetic field and a static field of 0.12 T. The ultimate compressive strength and Young's modulus of the scaffolds were measured in three directions: ice growth direction (Z), magnetic field direction (Y), and transverse direction (X). Sample size: $N=10$.

	Density	Porosity	Ultimate strength (MPa)			Young's modulus (MPa)		
	(g/cm^3)	(%)	X	Y	Z	X	Y	Z
0 wt% Fe_3O_4								
No field	0.53 ± 0.01	87.6 ± 0.1	0.6 ± 0.1	0.6 ± 0.1	4.7 ± 0.6	48 ± 24	48 ± 24	144 ± 55
Static field	–	–	–	–	–	–	–	–
1 wt% Fe_3O_4								
No field	0.55 ± 0.02	87.1 ± 0.5	1.1 ± 0.3	1.1 ± 0.3	8.9 ± 0.5	58 ± 25	58 ± 25	430 ± 92
Static field	0.55 ± 0.01	87.1 ± 0.3	1.4 ± 0.2	2.0 ± 0.5	9.0 ± 0.7	45 ± 30	142 ± 57	412 ± 139
3 wt% Fe_3O_4								
No field	0.51 ± 0.01	88.0 ± 0.3	0.9 ± 0.3	0.9 ± 0.3	7.4 ± 0.2	48 ± 20	48 ± 20	459 ± 74
Static field	0.52 ± 0.01	87.7 ± 0.2	1.4 ± 0.2	2.4 ± 0.6	6.3 ± 0.7	55 ± 29	117 ± 42	332 ± 95
9 wt% Fe_3O_4								
No field	0.47 ± 0.02	89.2 ± 0.4	0.8 ± 0.2	0.8 ± 0.2	5.0 ± 0.6	33 ± 8	33 ± 8	451 ± 74
Static field	0.47 ± 0.02	89.2 ± 0.4	0.9 ± 0.1	1.8 ± 0.3	3.2 ± 0.8	34 ± 8	113 ± 43	123 ± 50

*All data reported as average ± standard deviation.

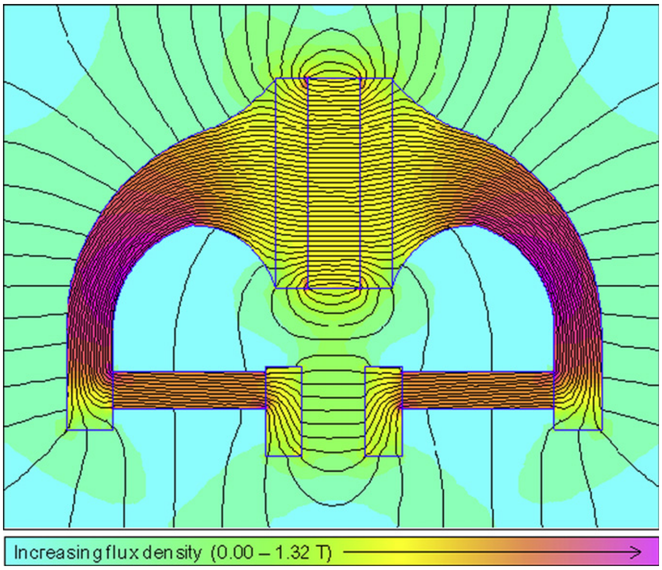

Fig. 2. Finite element model (FEM) showing the magnetic flux path and density distributions through the permanent magnet apparatus shown in Fig. 1. According to the legend (bottom), the highest flux density is shown in purple, while the lowest flux, density is shown in light blue. (For interpretation of the references to color in this figure legend, the reader is referred to the web version of this article.)

2.5. Microscopy

Optical microscopy images were taken with a VHX-1000 digital microscope system equipped with a CCD camera (KEYENCE Corporation, Osaka, Japan).

Scanning electron microscopy (SEM) images were taken at 10 kV on a Philips XL30 field emission environmental scanning electron microscope (FEI-XL30, FEI Company, Hillsboro, OR). For SEM preparation the samples were sputter-coated with iridium using an Emitech K575X sputter coater (Quorum Technologies Ltd., West Sussex, UK).

2.6. Mechanical testing

Compression testing of the TiO_2 scaffolds was performed on an Instron machine (Instron 3342, Norwood, MA) with a 500 N load cell at a crosshead velocity of 0.005 mm/s. The scaffolds were cut into small samples of approximately $5 \times 5 \times 5$ mm^3 and tested in three orthogonal directions (see Fig. 1): (1) ice growth direction (Z-axis); (2) magnetic flux path direction (Y-axis); and (3) transverse direction (X-axis). To ensure testing of the homogeneous region and avoid the high-density regions of the scaffolds (i.e., the outer perimeter and the bottom 5 mm of the scaffold [20]), the cubic samples were cut from the center core of the scaffolds (10×10 mm^2) between 5 and 30 mm from the bottom. The compressive ultimate strength and Young's modulus were determined from the maximum stress and the linear slope of the stress–strain curves, respectively.

3. Results and discussion

Directing a magnetic field through the ceramic slurries perpendicular to the ice growth direction was accomplished by channeling the field through the flux path distributors seen in Fig. 1. Fig. 2 shows a 2D finite element model (FEM) illustrating the magnetic field lines and density throughout the permanent magnet system. Measurements of the magnetic field strength using a Gauss meter and observations of the field direction using iron filaments in a clear test tube confirmed that the magnetic field through the PVC mold in the experiments described here was 0.12 T and normal to the freezing direction.

Fig. 3 shows images of freeze-cast HA, ZrO_2, Al_2O_3, and TiO_2 with 3 wt% (~3 vol%) Fe_3O_4 frozen at 10 °C/min under a rotating magnetic field of 0.12 T at 0.05 rpm. As seen in the images, the HA, ZrO_2, and Al_2O_3 scaffolds showed two distinct phases of the host ceramic (HA, ZrO_2, Al_2O_3) and Fe_3O_4 when fabricated under the influence of the external field. The TiO_2 scaffolds, on the other hand, did not show separate ceramic phases, suggesting that the Fe_3O_4 nanoparticles were well distributed and absorbed into the TiO_2 scaffold. Additionally, the Fe_3O_4 phase of the HA, ZrO_2, and Al_2O_3 scaffolds seemed to densify and deform the macrostructures after sintering (Fig. 3, right images).

Fig. 4 shows elemental mappings of the iron (Fe) concentration in sintered HA, ZrO_2, Al_2O_3, and TiO_2 scaffolds containing 3 wt% Fe_3O_4 made with a static magnetic field of 0.12 T. As seen in the elemental maps, gradients of varying Fe concentrations were observed in the HA, ZrO_2, and Al_2O_3 scaffolds (Fig. 4a–c). Alternatively, Fe in the TiO_2 scaffold was evenly distributed throughout (Fig. 4d). Table 2 shows measured concentrations of Fe and the host elements (Ca, P, Zr, Al, Ti, O) of each scaffold taken from Fig. 4. The *Fe_3O_4-rich region* was measured at the edges of the scaffolds closest to the poles of the external magnetic field, while the *Fe_3O_4-poor region* was measured at the center of the scaffolds

Please cite this article as: M.M. Porter, et al., Magnetic freeze casting inspired by nature, Materials Science & Engineering A (2012), http://dx.doi.org/10.1016/j.msea.2012.07.058

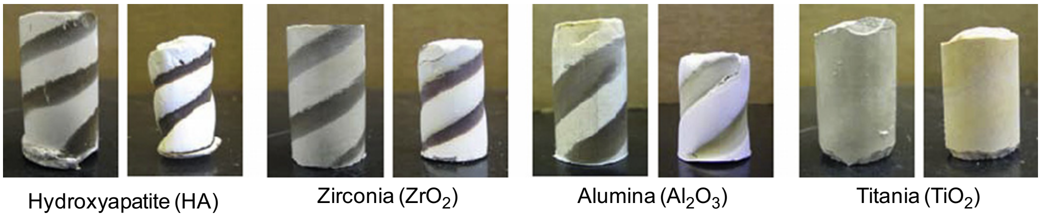

Fig. 3. Images of different ceramic scaffolds containing 3 wt% (∼3 vol%) Fe_3O_4 nanoparticles made with a rotating magnetic field of 0.12 T at 0.05 rpm. Left images of each scaffold were taken after lyophilizing and before sintering. Right images were taken after, sintering for 3 h at predetermined temperatures of 1300 °C for HA and ZrO_2, 1500 °C for Al_2O_3, and 900 °C for TiO_2. All scaffolds, before sintering were 20 mm in diameter.

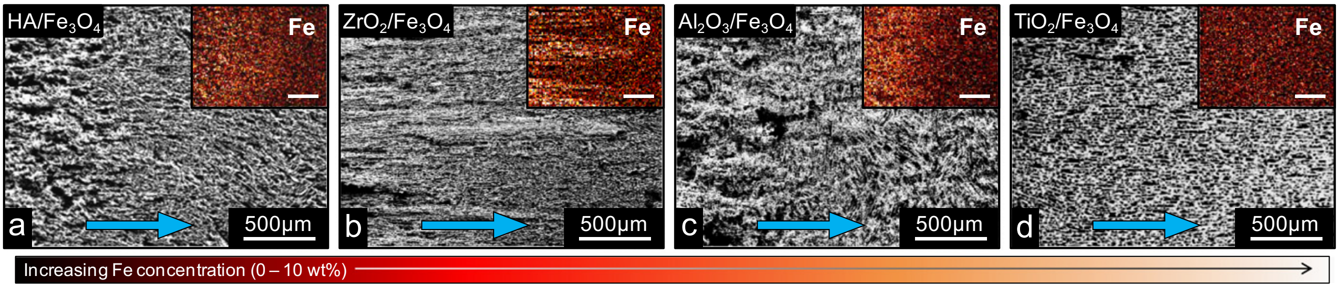

Fig. 4. Elemental mapping of iron (Fe) concentration in sintered (a) HA, (b) ZrO_2, (c) Al_2O_3, and (d) TiO_2 scaffolds containing 3 wt% (∼3 vol%) Fe_3O_4 made with a static magnetic field of 0.12 T. According to the legend (bottom), the highest concentration of Fe is shown in white, while the lowest concentration of Fe is shown in black. Images were taken in the transverse *XY*-plane, perpendicular to the direction of ice growth. The magnetic field direction is shown with blue, horizontal arrows. All scale bars are 500 µm.

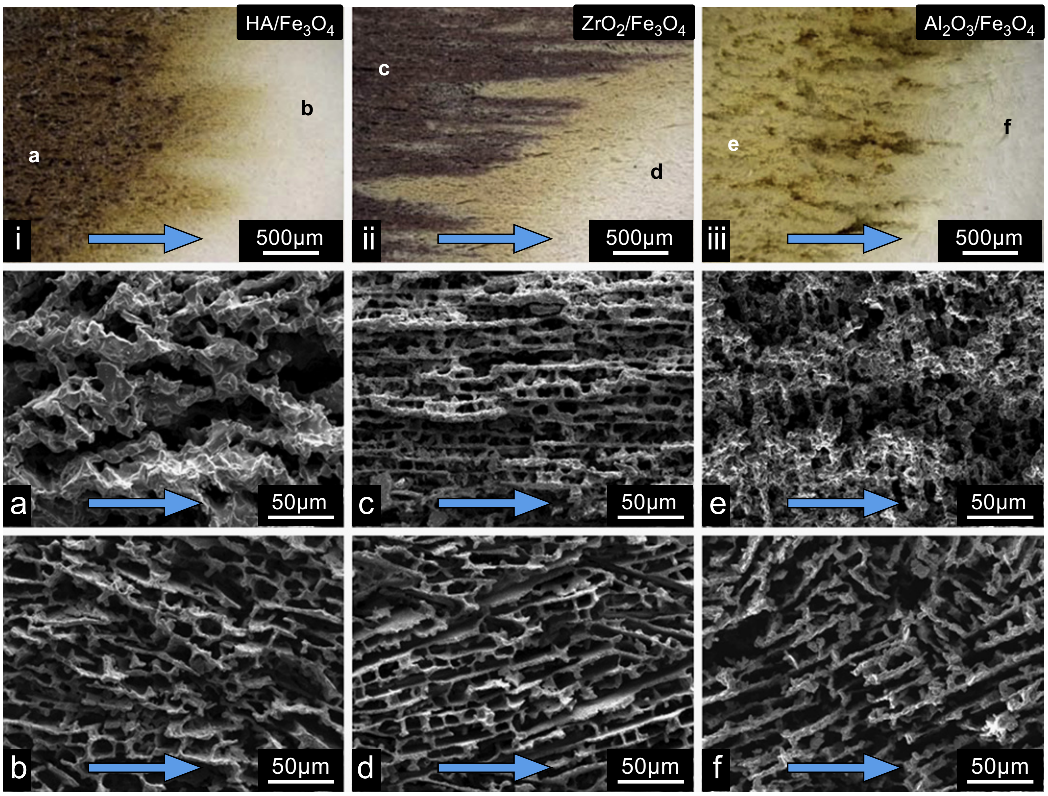

Fig. 5. From left to right, micrographs of sintered HA, ZrO_2, and Al_2O_3 scaffolds containing 3 wt% (∼3 vol%) Fe_3O_4 made with a static magnetic field of 0.12 T. ((i)–(iii)) Optical images of the different scaffolds showing the Fe_3O_4 phase transitions. ((a), (c) and (e)) Magnified SEM images of the Fe_3O_4-rich regions. ((b), (d) and (f)) Magnified SEM images of the Fe_3O_4-poor regions. All images were taken in the transverse *XY*-plane, perpendicular to the direction of ice growth. Images ((i)–(iii)) show the locations of images ((a)–(f)), respectively. The magnetic field direction is shown with blue, horizontal arrows. All micrographs were imaged at 15 mm from the bottom of the scaffolds.

away from the poles of the external field. It is apparent that the Fe concentrations in the Fe_3O_4-rich and Fe_3O_4-poor regions of the TiO_2 scaffold were nearly equal. However, the highest concentrations of Fe in the HA, ZrO_2, and Al_2O_3 scaffolds were located at the edges (Fe_3O_4-rich region), closest to the poles of the external magnetic field.

Fig. 5 contains magnified optical and SEM micrographs of the sintered HA, ZrO_2, and Al_2O_3 scaffolds made with a static magnetic field of 0.12 T. In the optical images (Fig. 5i–iii), the distribution of color further suggests that the Fe_3O_4 (brown/purple/yellow) concentrated to the poles of the magnetic field and separated from the host ceramic (white). The microstructures of the Fe_3O_4-rich (brown/purple/yellow) and Fe_3O_4-poor (white) regions are distinctly different. The Fe_3O_4-rich HA (Fig. 5a) has thick lamellar walls and large pores (20–50 μm), while the Fe_3O_4-poor HA (Fig. 5b) has thin lamellar walls and small pores (10–20 μm), similar to a pure HA scaffold. The Fe_3O_4-rich ZrO_2 (Fig. 5c) is more dense with narrow lamellar walls aligned in the direction of the magnetic field. The Fe_3O_4-poor ZrO_2 (Fig. 5d) is a porous structure with random alignment, similar to a pure ZrO_2 scaffold. The Fe_3O_4-rich Al_2O_3 (Fig. 5e) has a dense microstructure with larger ridges aligned in the direction of the magnetic field, while the Fe_3O_4-poor Al_2O_3 (Fig. 5f) has a random alignment similar to a pure Al_2O_3 scaffold. This biphasic behavior was not observed in the scaffolds made with no magnetic field. Instead, the two phases were well mixed and evenly distributed throughout, resulting in the homogeneous microstructures shown in Fig. 6a–c.

Table 1 lists the physical properties of the ceramic powders in the as-received condition. Although the driving forces behind the Fe_3O_4-host, particle-particle interactions observed in Fig. 4 are not fully understood, it is known that the motion of magnetic and nonmagnetic particles in a colloidal suspension under an external magnetic field is governed by magnetic dipole, electrostatic, van der Waals, and hydrodynamic forces [47–49]. Brownian motion, which dominates collisions of colloidal particles <1 μm, is dependent on the concentration, size, and density of the particles [47]. There seems to be no relation linking the initial particle size or molar mass to the biphasic behaviors observed in Fig. 4a–c (compare with Table 1). Therefore, it may be reasonable to assume that the similar densities of the Fe_3O_4 (4.95 g/cm^3) and TiO_2 (4.26 g/cm^3) would allow for the homogeneous mixing seen in Fig. 4d. The different crystal systems may also play a role in the particle-particle interactions observed, but this has yet to be determined. Though it may be useful to develop composite materials such as those with two distinct phases (Fig. 5), this was not main objective of this work. Thus, the remainder of this paper focuses on the physical and mechanical properties of the TiO_2 scaffolds.

X-ray diffraction patterns of TiO_2 scaffolds containing 3 wt% Fe_3O_4 (Fig. 7) show that the crystal structure of the TiO_2 transformed from anatase before sintering to rutile after sintering at 900 °C. It is also apparent in Fig. 7 that the Fe_3O_4 initially present before sintering was absorbed into the TiO_2 scaffolds after sintering, forming a small amount of the iron titanium oxide, pseudobrookite (Fe_2TiO_5).

Fig. 8 shows SEM micrographs of TiO_2 scaffolds containing 3 wt% Fe_3O_4 produced with no magnetic field (top), a static magnetic field (center), and a rotating magnetic field (bottom). The scaffolds made with no magnetic field showed directional alignment only in the longitudinal ice growth direction, represented by a green arrow. Fig. 8a shows the edges and some faces of lamellar sheets oriented in the longitudinal YZ-plane. In the transverse XY-plane (Fig. 8b), there is no uniform alignment of the micro-channels, but several small domains (~100–500 μm) of similarly oriented channels—an intrinsic property of most freeze-cast ceramics [27,50,51]. Scaffolds made with a static field of 0.12 T showed directional alignment in both the longitudinal (Fig. 8c) and transverse (Fig. 8d) planes. The weak magnetic field, represented by a blue arrow, introduced some order of channel alignment parallel to the field direction. Fig. 8c shows the faces of lamellar sheets propagating along the longitudinal ice growth direction (green arrow). The magnetic field (blue arrow) forced the lamellar sheets in orientations along the field direction. Although not all the lamellar sheets were aligned throughout the entire scaffold, a vast majority of the micro-channels showed preferred alignments parallel to the field direction, resulting in large domains ($\gg 500\ \mu m$) of similarly oriented channels, as seen in Fig. 8d. Scaffolds made with a rotating magnetic field of 0.12 T at 0.05 rpm also showed some order of alignment in the longitudinal (Fig. 8e) and transverse (Fig. 8f) planes. The lamellar sheets of the scaffolds with a rotating field seemed to be skewed by the field rotation, resulting in slanted lamellar sheets oriented ~30° off-axis from the ice growth direction (green arrow), seen in Fig. 8e. Long-range alignment of the micro-channels (10–20 μm pores) in the transverse plane was not apparent in the scaffolds made with a rotating field. Instead, aligned macro-channels (~50 μm pores) were created by the magnetic field rotation. Fig. 9 shows μCT images of a sintered TiO_2 scaffold containing 3 wt% Fe_3O_4 made with a rotating magnetic field. The 3D

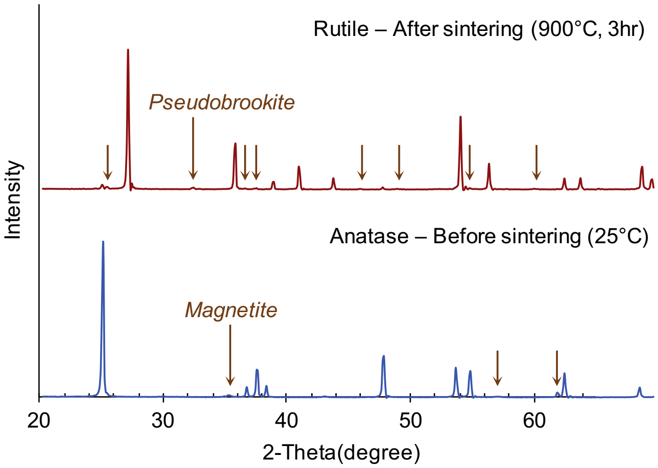

Fig. 7. X-ray diffraction (XRD) patterns of TiO_2 scaffolds containing 3 wt% (~3 vol%) Fe_3O_4 before and after sintering at 900 °C for 3 h. Before sintering the TiO_2 is anatase (blue) and after sintering the TiO_2 is rutile (red). Peaks corresponding to magnetite (Fe_3O_4) and pseudobrookite (Fe_2TiO_5) are marked by the arrows in the XRD patterns before and after sintering, respectively. (For interpretation of the references to color in this figure legend, the reader is referred to the web version of this article.)

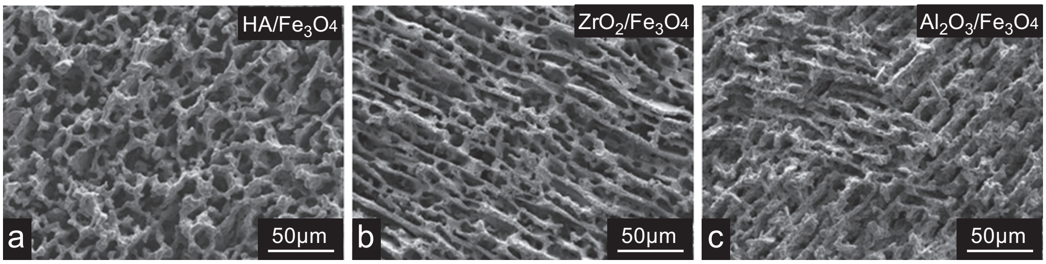

Fig. 6. Micrographs of sintered (a) HA, (b) ZrO_2, and (c) Al_2O_3 scaffolds containing 3 wt% (~3 vol%) Fe_3O_4 made with no magnetic field. All micrographs were imaged at 15 mm from the bottom of the scaffolds.

Please cite this article as: M.M. Porter, et al., Magnetic freeze casting inspired by nature, Materials Science & Engineering A (2012), http://dx.doi.org/10.1016/j.msea.2012.07.058

reconstruction (Fig. 9a) and top view (Fig. 9b) of the scaffold show a spiraling perimeter of higher density material. This helicoidal, high-density perimeter may add torsional rigidity to the scaffold. Fig. 9c shows the larger macro-channels aligned in the direction of the magnetic field (blue arrow). Interestingly, these macro-channels did not appear in the scaffolds made with no magnetic field or a static magnetic field. It seems that the subtle movements and realignments of the Fe_3O_4 particles caused by the field rotation at the freezing front disrupted the uniformity of ice crystal growth, resulting in the macro-channels observed in Fig. 9c. The high-density perimeter seen in Fig. 9b, however, was similarly observed in the scaffolds made with a static field, showing a slightly higher density at the edges adjacent to the magnet poles.

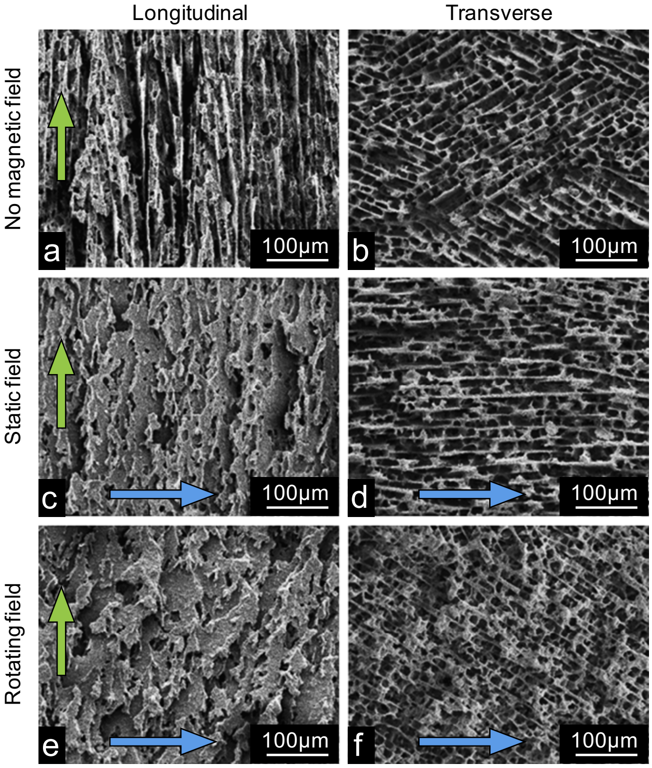

Fig. 8. SEM micrographs of TiO_2 scaffolds containing 3 wt% (~3 vol%) Fe_3O_4 made with no magnetic field (top), a static magnetic field of 0.12 T (center), and a rotating magnetic field of 0.12 T at 0.05 rpm (bottom). Left images show microstructures in the longitudinal *YZ*-plane. Right images show microstructures in the transverse *XY*-plane. The ice growth direction is shown with green, vertical arrows. The magnetic field direction is shown with blue, horizontal arrows. All micrographs were imaged at 15 mm from the bottom of the scaffolds. (For interpretation of the references to color in this figure legend, the reader is referred to the web version of this article.)

Compression tests on the TiO_2 scaffolds were preformed on samples cut from the central region of the cylindrical scaffolds ($10 \times 10\ mm^2$) to avoid any edge effects from the high-density perimeters. Fig. 10 displays the results from compression tests on TiO_2 scaffolds with 3 wt% Fe_3O_4 made with no magnetic field (dotted lines, orange bars) and a static magnetic field of 0.12 T (solid lines, purple bars). As seen in the representative stress–strain plot (Fig. 10a), the ultimate compressive strength of the scaffolds made with no field (dotted lines) was ~7.5 MPa in the ice growth direction (*Z*) and <1 MPa in the transverse plane (*X*, *Y*). When the scaffolds were fabricated under a static field (solid lines), the strength in the ice growth direction (*Z*) decreased slightly to ~6.5 MPa. Nevertheless, the strength and modulus in the direction of the magnetic field (*Y*) was more than doubled! Fig. 10b and c show the increases in compressive strength and stiffness of the scaffolds made with a static magnetic field, respectively. The directional alignment of the micro-channels in the scaffolds made with a static field (Fig. 8d) added significant strength and stiffness in the direction of the magnetic field.

To see the effect of Fe_3O_4 on the TiO_2 scaffolds, several samples with varying concentrations of 0–9 wt% (0–8 vol%) Fe_3O_4 were prepared and tested. Fig. 11 contains plots of the strength and modulus in the magnetic field (*Y*) and ice growth (*Z*) directions versus initial concentration of Fe_3O_4 (wt%). As seen in Fig. 11a and b, introducing a static magnetic field of 0.12 T doubled both the strength and modulus of the scaffolds containing 1–9 wt% Fe_3O_4 in the magnetic field direction (*Y*). The strength and modulus in the ice growth direction (*Z*), on the other hand, decreased with the introduction of a static magnetic field and increasing Fe_3O_4 (Fig. 11c and d). Table 3 summarizes the physical and mechanical properties of the TiO_2 scaffolds containing 0–9 wt% Fe_3O_4. The decrease in strength and stiffness of the TiO_2 scaffolds in the ice growth direction (*Z*) with increasing Fe_3O_4 concentration seems to be related to the decrease in density, and corresponding increase in porosity, of the scaffolds (Table 3). This trend is most likely related to the sintering characteristics of the two phases. Fig. 12 shows SEM micrographs of the lamellar wall surfaces of TiO_2 scaffolds containing 0–9 wt% Fe_3O_4 sintered at 900 °C. As seen in Fig. 12a, the TiO_2 scaffold containing 0 wt% Fe_3O_4 is composed of small particles $\ll 500$ nm. The TiO_2 scaffolds made with 1–9 wt% Fe_3O_4 showed significant grain growth with larger rod-like particles $\gg 500$ nm (Fig. 12b–d). This observation is consistent with the fact that iron additives may be used as sintering aids in ceramics processing to promote grain growth and agglomeration [52,53]. Adding Fe_3O_4 to the TiO_2 scaffolds

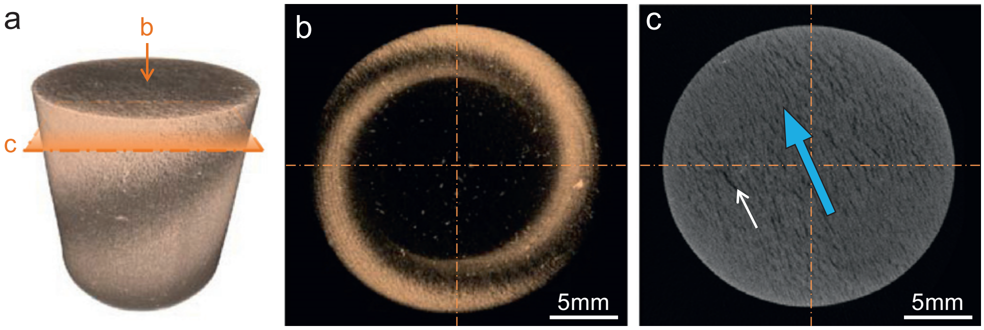

Fig. 9. Micro-computed tomography images of a sintered TiO_2 scaffold containing 3 wt% (~3 vol%) Fe_3O_4 made with a rotating magnetic field of 0.12 T at 0.05 rpm. (a) 3D reconstruction of the scaffold showing the high-density (dark brown) and low-density (light brown) regions. (b) Top view of the scaffold with opacity adjusted to show only the high-density regions around the perimeter of the scaffold. (c) Image of the transverse *XY*-plane perpendicular to the ice growth direction at 20 mm from the bottom of the scaffold. The magnetic field direction is shown with the blue arrow. An aligned macro-channel (~50 μm wide) is noted with the white arrow. (For interpretation of the references to color in this figure legend, the reader is referred to the web version of this article.)

Please cite this article as: M.M. Porter, et al., Magnetic freeze casting inspired by nature, Materials Science & Engineering A (2012), http://dx.doi.org/10.1016/j.msea.2012.07.058

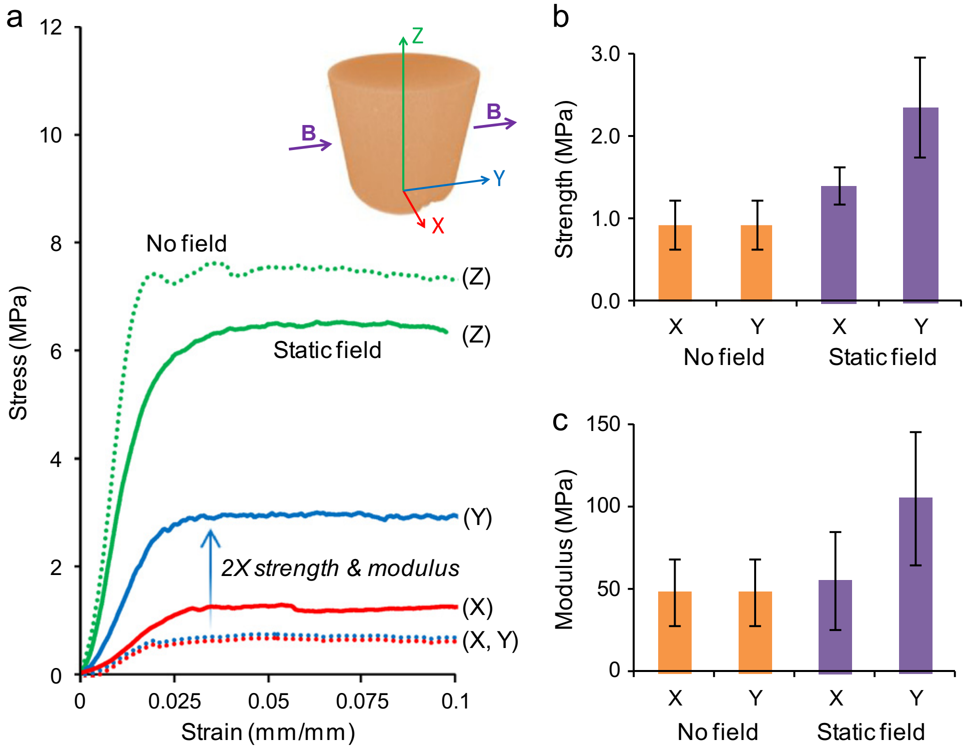

Fig. 10. Compressive mechanical properties of TiO_2 scaffolds containing 3 wt% (~3 vol%) Fe_3O_4. (a) Representative stress–strain curves for the scaffolds made with no magnetic field (dotted lines) and a static magnetic field of 0.12 T (solid lines). Compression tests were performed in three directions (see top schematic): ice growth direction (*Z*, green), magnetic field direction (*Y*, blue), and transverse direction (*X*, red). (b) Ultimate compressive strength and (c) Young's modulus in the transverse *XY*-plane of the scaffolds made with no magnetic field (orange) and a static magnetic field of 0.12 T (purple). (For interpretation of the references to color in this figure legend, the reader is referred to the web version of this article.)

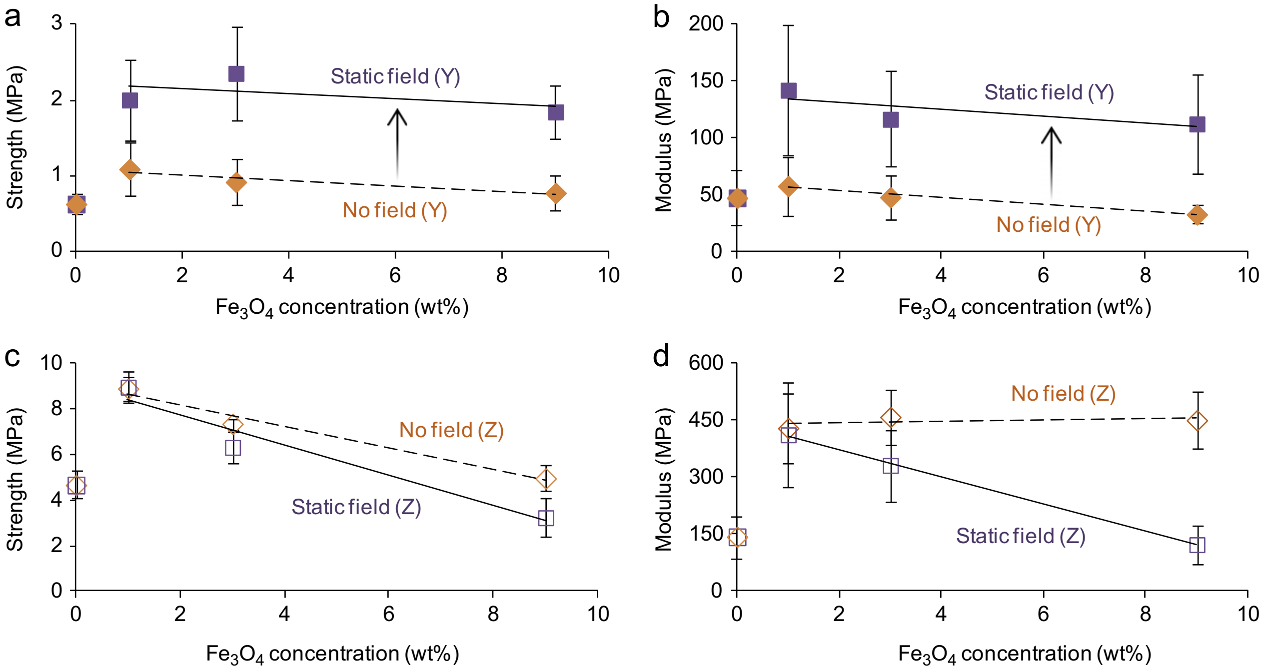

Fig. 11. Compressive mechanical properties of TiO_2 scaffolds containing 0–9 wt% (0–8 vol%) Fe_3O_4 produced with no magnetic field (orange diamonds, dashed trend line) and a static magnetic field of 0.12 T (purple squares, solid trend line). ((a) and (b)) Ultimate strength and Young's modulus of scaffolds in the magnetic field direction (*Y*). Black arrows indicate an increase in strength and modulus in the transverse *Y*-direction due to the static magnetic field. ((c) and (d)) Ultimate strength and Young's modulus of scaffolds in the ice growth direction (*Z*).

increased the strength and stiffness at low iron concentrations with and without a magnetic field (Table 3). In the magnetic field direction (*Y*), increasing the Fe_3O_4 concentration from 1 to 9 wt% had very little effect on the resulting mechanical properties (Fig. 11a and b). Conversely, increasing the concentration of Fe_3O_4 from 1 to 9 wt% decreased the strength and stiffness of the scaffolds in the ice growth direction (*Z*), especially when fabricated under a static magnetic field (Fig. 11c and d). The

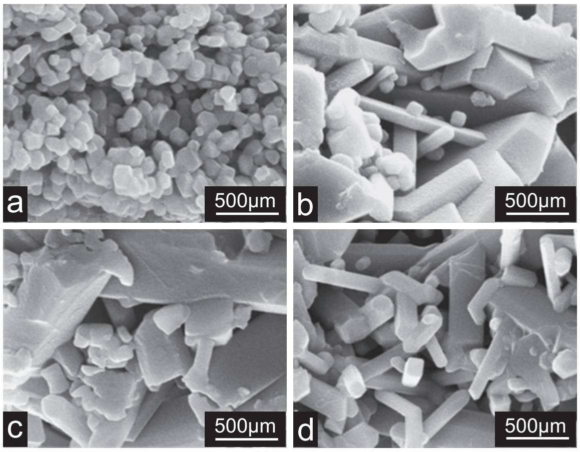

Fig. 12. SEM micrographs of the lamellar wall surfaces of TiO_2 scaffolds sintered at 900 °C, containing varying concentrations of Fe_3O_4: (a) 0 wt% Fe3O4; (b) 1 wt% (~1 vol%) Fe_3O_4; (c) 3 wt% (~3 vol%) Fe_3O_4; (d) 9 wt% (~8 vol%) Fe_3O_4.

normal, directional alignment caused by the magnetic field seems to have disrupted some of the long-range order produced by the growing ice lamellae, which led to a decrease of mechanical integrity in the longitudinal, ice growth direction.

The unusual phenomenon of decreasing density with increasing Fe_3O_4 concentrations (Table 3) agrees with observations reported by Zhang et al. [54] that an increase in iron-doping (atom% Fe) of TiO_2 arrests nanocrystalline particle growth at increased temperatures (> 500 °C). Although iron additives can promote grain growth during sintering, high concentrations of iron (> 1 wt%) in the TiO_2 scaffolds may limit the size increase of nanocrystalline particles, which in turn, inhibits densification and diminishes the mechanical properties. Therefore, increasing the Fe_3O_4 concentration decreased the density, strength, and stiffness of the TiO_2 scaffolds in the ice growth direction, but not the magnetic field direction. The optimal concentration of Fe_3O_4 added to the TiO_2 scaffolds is ~1 wt%, since the mechanical properties are nearly doubled in the magnetic field direction (Y) and remain unchanged in the ice growth direction (Z) with the introduction of a static magnetic field of 0.12 T.

4. Conclusions

Magnetic field aligned freeze casting is a new method to fabricate anisotropic ceramic scaffolds with highly porous, directionally aligned microstructures. The addition of an external magnetic field to a conventional freeze casting unit allows the interconnected pore channels to be aligned in two directions: (1) the ice growth direction and (2) the magnetic field direction.

A variety of ceramic materials can be freeze cast into porous scaffolds. Under the influence of a weak magnetic field (0.12 T), the inter-particle interactions between the Fe_3O_4 nanoparticles and the host ceramic (hydroxyapatite (HA), ZrO_2, Al_2O_3, or TiO_2) determine the final microstructures and mechanical properties of the freeze-cast scaffolds. Fe_3O_4 was well distributed throughout the TiO_2 scaffolds, but separated into distinctly different phases in the HA, ZrO_2, and Al_2O_3 scaffolds. The TiO_2 scaffolds fabricated with a static magnetic field showed channel alignment in, not only the ice growth direction, but also the magnetic field direction. The directional order induced by the static field doubled both the strength and modulus in the magnetic field direction of the TiO_2 scaffolds containing 1–9 wt% Fe_3O_4. The mechanical properties in the ice growth direction decreased by adding a magnetic field and increasing the Fe_3O_4 concentration. Even so, the loss in strength and stiffness in the ice growth direction was insignificant compared to the gain measured in the magnetic field direction at low Fe_3O_4 concentrations (1 wt%).

The concept of magnetic freeze casting may be used in a variety of future applications. The magnetic field strength and rotation speed may be adjusted to introduce varying degrees of micro-/macro-channel alignment or spiraling regions of high-density reinforced perimeters (Fig. 9b) to make scaffolds with exceptional torsional rigidity. Scaffolds composed of feeble magnetic ceramics, such as HA or Al_2O_3, may be aligned similar the TiO_2 scaffolds reported here by coating magnetic nanoparticles before freezing. High aspect ratio nanowires or nanotubes may be added and aligned in a ceramic slurry to create “nano-bridges” between adjacent lamellae for enhanced strength and toughness. Conductive nanostructures, such as carbon nanotubes or metallic nanoparticles, may be added and aligned to improve the conductivity of scaffolds for potential electronic and energy storage devices. Finally, magnetic hybrid composites could be fabricated as high-performance, multifunctional materials for a variety of structural or medical applications.

Acknowledgements

The authors would like to thank Dr. Antoni Tomsia at the Lawrence Berkeley National Laboratory for generously opening his laboratory to us and teaching us the technical details of freeze casting. Prof. Nathan Delson of Mechanical and Aerospace Engineering, UCSD, and Steve Lee of Materials Science and Engineering, UCSD, are thanked for their assistant in the development and fabrication of the magnetic freeze casting apparatus. Dr. Esther Cory and Prof. Robert Sah of Bioengineering, UCSD, guided analysis of the μCT scans. This work is supported by the National Science Foundation, Division of Materials Research, Ceramics Program Grant, 1006931.

References

[1] P.Y. Chen, A.Y.M. Lin, Y.S. Lin, Y. Seki, A.G. Stokes, J. Peyras, E.A. Olevsky, M.A. Meyers, J. McKittrick, J. Mech. Behav. Biomed. Mater. 1 (2008) 208–226.
[2] M.A. Meyers, P.Y. Chen, A.Y.M. Lin, Y. Seki, Prog. Mater. Sci. 53 (2008) 1–206.
[3] U.G.K. Wegst, M.F. Ashby, Philos. Mag. 84 (2004) 2167–2181.
[4] J.D. Currey, Bones: Structure and Mechanics, Princeton University Press, Princeton, NJ, 2002.
[5] X.D. Li, W.C. Chang, Y.J. Chao, R.Z. Wang, M. Chang, Nano Lett. 4 (2004) 613–617.
[6] S. Deville, Adv. Eng. Mater. 10 (2008) 155–169.
[7] W.L. Li, K. Lu, J.Y. Walz, Int. Mater. Rev. 57 (2012) 37–60.
[8] S. Deville, E. Saiz, A.P. Tomsia, Biomaterials 27 (2006) 5480–5489.
[9] Q. Fu, M.N. Rahaman, F. Dogan, B.S. Bal, Biomed. Mater. 3 (2008).
[10] S. Lee, M. Porter, S. Wasko, G. Lau, P.-Y. Chen, E.E. Novitskaya, A.P. Tomsia, A. Almutairi, M.A. Meyers, J. McKittrick, 2011 MRS Fall Meeting and Exhibit, Materials Research Society, Boston, 2011, in.
[11] S. Deville, E. Saiz, R.K. Nalla, A.P. Tomsia, Science 311 (2006) 515–518.
[12] M.E. Launey, E. Munch, D.H. Alsem, H.B. Barth, E. Saiz, A.P. Tomsia, R.O. Ritchie, Acta Mater. 57 (2009) 2919–2932.
[13] E. Munch, M.E. Launey, D.H. Alsem, E. Saiz, A.P. Tomsia, R.O. Ritchie, Science 322 (2008) 1516–1520.
[14] K. Araki, J.W. Halloran, J. Am. Ceram. Soc. 88 (2005) 1108–1114.
[15] T. Fukasawa, Z.Y. Deng, M. Ando, T. Ohji, S. Kanzaki, J. Am. Ceram. Soc. 85 (2002) 2151–2155.
[16] S.H. Lee, S.H. Jun, H.E. Kim, Y.H. Koh, J. Am. Ceram. Soc. 91 (2008) 1912–1915.
[17] T. Moritz, H.J. Richter, J. Eur. Ceram. Soc. 27 (2007) 4595–4601.
[18] U.G.K. Wegst, M. Schecter, A.E. Donius, P.M. Hunger, Philos. Trans. R. Soc. A-Math. Phys. Eng. Sci. 368 (2010) 2099–2121.
[19] S. Deville, E. Maire, G. Bernard-Granger, A. Lasalle, A. Bogner, C. Gauthier, J. Leloup, C. Guizard, Nat. Mater. 8 (2009) 966–972.
[20] S. Deville, E. Saiz, A.P. Tomsia, Acta Mater. 55 (2007) 1965–1974.
[21] Q. Fu, M.N. Rahaman, F. Dogan, B.S. Bal, J. Biomed. Mater. Res. Part B 86B (2008) 125–135.
[22] Q. Fu, M.N. Rahaman, F. Dogan, B.S. Bal, J. Biomed. Mater. Res. Part B 86B (2008) 514–522.
[23] Y.H. Koh, J.H. Song, E.J. Lee, H.E. Kim, J. Am. Ceram. Soc. 89 (2006) 3089–3093.
[24] A. Macchetta, I.G. Turner, C.R. Bowen, Acta Biomater. 5 (2009) 1319–1327.

Please cite this article as: M.M. Porter, et al., Magnetic freeze casting inspired by nature, Materials Science & Engineering A (2012), http://dx.doi.org/10.1016/j.msea.2012.07.058

[25] J.W. Moon, H.J. Hwang, M. Awano, K. Maeda, Mater. Lett. 57 (2003) 1428–1434.
[26] E. Munch, J. Franco, S. Deville, P. Hunger, E. Saiz, A.P. Tomsia, J. Oper. Manag. 60 (2008) 54–58.
[27] E. Munch, E. Saiz, A.P. Tomsia, S. Deville, J. Am. Ceram. Soc. 92 (2009) 1534–1539.
[28] T. Waschkies, R. Oberacker, M.J. Hoffmann, J. Am. Ceram. Soc. 92 (2009) S79–S84.
[29] J.L. Zou, Y. Zhang, R.X. Li, Int. J. Appl. Ceram. Technol. 8 (2011) 482–489.
[30] Y.H. Koh, E.J. Lee, B.H. Yoon, J.H. Song, H.E. Kim, H.W. Kim, J. Am. Ceram. Soc. 89 (2006) 3646–3653.
[31] Y.M. Zhang, L.Y. Hu, J.C. Han, J. Am. Ceram. Soc. 92 (2009) 1874–1876.
[32] M.A. Correa-Duarte, M. Grzelczak, V. Salgueirino-Maceira, M. Giersig, L.M. Liz-Marzan, M. Farle, K. Sierazdki, R. Diaz, J. Phys. Chem. B 109 (2005) 19060–19063.
[33] M. Horton, H.P. Hong, C. Li, B. Shi, G.P. Peterson, S.H. Jin, J. Appl. Phys. 107 (2010).
[34] M. Mashkour, M. Tajvidi, T. Kimura, F. Kimura, G. Ebrahimi, BioResources 6 (2011) 4731–4738.
[35] J. Tumpane, N. Karousis, N. Tagmatarchis, B. Norden, Angew. Chem. Int. Ed. 47 (2008) 5148–5152.
[36] H. Wang, Q.W. Chen, L.X. Sun, H.P. Qi, X. Yang, S. Zhou, J. Xiong, Langmuir 25 (2009) 7135–7139.
[37] Y.Y. Xu, J.Y. Yuan, B. Fang, M. Drechsler, M. Mullner, S. Bolisetty, M. Ballauff, A.H.E. Muller, Adv. Funct. Mater. 20 (2010) 4182–4189.
[38] K. Yamaguchi, K. Matsumoto, T. Fujii, J. Appl. Phys. 67 (1990) 4493–4495.
[39] J. Akiyama, M. Hashimoto, H. Takadama, F. Nagata, Y. Yokogawa, K. Sassa, K. Iwai, S. Asai, Formation of *c*-axis aligned hydroxyapatite sheet by simultaneous imposition of high magnetic field and mold rotation during slip casting process, in: T. Nakamura, K. Yamashita, M. Neo (Eds.), Bioceramics 18, Pts 1 and 2, Trans Tech Publications Ltd, Zurich-Uetikon, 2006, pp. 53–56.
[40] Y. Sakka, T.S. Suzuki, J. Ceram. Soc. Jpn. 113 (2005) 26–36.
[41] T.S. Suzuki, T. Uchikoshi, Y. Sakka, Sci. Technol. Adv. Mater. 7 (2006) 356–364.
[42] T.S. Suzuki, T. Uchikoshi, Y. Sakka, J. Ceram. Soc. Jpn. 119 (2011) 334–337.
[43] F.Q. Tang, T. Uchikoshi, T.S. Suzuki, Y. Sakka, Mater. Res. Bull. 39 (2004) 2155–2161.
[44] T. Uchikoshi, T.S. Suzuki, S. Iimura, F.Q. Tang, Y. Sakka, J. Eur. Ceram. Soc. 26 (2006) 559–563.
[45] C. Wu, K. Sassa, K. Iwai, S. Asai, Mater. Lett. 61 (2007) 1567–1571.
[46] D. Ficai, A. Ficai, B.S. Vasile, M. Ficai, O. Oprea, C. Guran, E. Andronescu, Dig. J. Nanomater. Biostruct. 6 (2011) 943–951.
[47] C.J. Chin, S.C. Lu, S. Yiacoumi, C. Tsouris, Sep. Sci. Technol. 39 (2004) 2839–2862.
[48] X.L. Peng, Y. Min, T.Y. Ma, W. Luo, M. Yan, J. Magn. Magn. Mater. 321 (2009) 1221–1226.
[49] X.L. Peng, Y. Min, T.Y. Ma, M. Yan, J. Magn. Magn. Mater. 321 (2009) 3250–3255.
[50] S. Deville, E. Maire, A. Lasalle, A. Bogner, C. Gauthier, J. Leloup, C. Guizard, J. Am. Ceram. Soc. 92 (2009) 2489–2496.
[51] S. Deville, E. Maire, A. Lasalle, A. Bogner, C. Gauthier, J. Leloup, C. Guizard, J. Am. Ceram. Soc. 92 (2009) 2497–2503.
[52] M.A. Einarsrud, E. Hagen, G. Pettersen, T. Grande, J. Am. Ceram. Soc. 80 (1997) 3013–3020.
[53] F.P. Filho, R. Nogueira, M.Y.F. Graca, M.A. Valente, A.S.B. Sombra, C.C. Silva, Physica B 403 (2008) 3826–3829.
[54] Y.H. Zhang, A. Reller, J. Mater. Chem. 11 (2001) 2537–2541.

Please cite this article as: M.M. Porter, et al., Magnetic freeze casting inspired by nature, Materials Science & Engineering A (2012), http://dx.doi.org/10.1016/j.msea.2012.07.058